We are IntechOpen,
the world's leading publisher of
Open Access books
Built by scientists, for scientists

6,900
Open access books available

186,000
International authors and editors

200M
Downloads

Our authors are among the

154
Countries delivered to

TOP 1%
most cited scientists

12.2%
Contributors from top 500 universities

CLARIVATE ANALYTICS
BOOK CITATION INDEX
INDEXED

WEB OF SCIENCE™

Selection of our books indexed in the Book Citation Index
in Web of Science™ Core Collection (BKCI)

Interested in publishing with us?
Contact book.department@intechopen.com

A Combined Electric/Magnetic Field Surface Volume Integral Equation Approach for the Fast Characterization of Microstrip/Substrate Integrated Waveguide Structures and Antennas

Thomas Vaupel

Additional information is available at the end of the chapter

Abstract

In this contribution, a combined electric field/magnetic field surface/volume integral equation approach is presented with special features for the characterization of substrate integrated waveguide (SIW) components. Due to the use of a parallel-plate waveguide Green's function, only a small number of volume current basis functions are necessary to model the vias of the SIW sidewalls. The focal point is set on the specification of microstrip-SIW transitions using a via and a pad/antipad configuration for the coupling between the microstrip parts and the SIW and transitions with a two-stage ridged substrate integrated waveguide (SIW) where the SIW has a very thick substrate with regard to the microstrip line making it well suited for the design of a new class of compact end-fire SIW antennas for phased array applications which are partly characterized with CST Microwave Studio. An effective S-parameter extraction is used with both microstrip and special SIW waveguide ports.

Keywords: integral equation, surface/volume discretization, microstrip-SIW transitions, S-parameter extraction, via and slot modeling, horn, slot/leaky wave antennas

1. Introduction

Due to the trend to higher frequencies, substrate integrated waveguide (SIW) components and antennas are once more well-suited building blocks to realize applications with low losses and compact design. A SIW consists of two periodic rows of metallic vias connecting metallic strips (or ground planes) on top and bottom of a dielectric substrate as a quasi-planar structure and

can thus very easily integrated and fabricated together with other microstrip/coplanar components using standard printed circuit board technologies and can be considered as a filled rectangular waveguide with the via rows as sidewalls [3]. Therefore, SIWs have the same low loss properties and first designs can be made using tools for the calculation of rectangular waveguide components. Thus, SIWs are increasingly used for antenna feeding networks with power dividers, filters, resonators, couplers, and phase shifters in micro- and mm-wave applications. For the full-wave characterization of such components, frequently mode matching techniques are proposed, but they are typically restricted to the modeling of the SIW components itself but without considering transitions to a microstrip/coplanar environment or radiating slot elements [2]. At the moment a strong interest is set on compact broadband horn-like SIW antennas with end-fire radiation characteristic [10, 11]. However, to reach the desired broadband properties with compact dimensions suited for phased array applications, SIWs on a thick substrate are needed. Simple microstrip-SIW transitions or interconnects like in [3, 6] cannot be used for the excitation of such thick SIWs; in this context, tapered transitions in vertical and lateral direction are proposed in [4]. In contrast to this, we have presented a two-stage transition based on a Chebychef design in [5]. Since the fabrication of the ridged-SIW structures is quite elaborate, we have also investigated transitions using a shorted via between the microstrip line and the bottom of the SIW as given in [6]. Such structure can be easily fabricated, but the bandwidth becomes small using thicker substrates. For thick substrates we investigate transitions where the length of the coupling via is smaller than the SIW thickness like the typical probes in standard rectangular waveguides. For the characterization of these structures, we have extended an integral equation approach [7] with special features for the effective characterization of SIWs. Based on the Green's functions of multilayered media, a substrate-filled parallel-plate medium can be used in many cases; thus together with volume basis functions for vertical currents, only the vias of the SIWs must be discretized. The microstrip parts are modeled with electric surface currents, whereas the antipads and other apertures are modeled with magnetic surface currents allowing the characterization of a class of leaky wave antennas [8] with very low computational effort. A further task was the careful S-parameter determination comprising both microstrip- and SIW waveguide ports.

2. Formulation with first applications

The round vias of SIW structures with diameter d_{circ} can be replaced for the simulations by quadratic vias with the side length l_{square} with typically high accuracy using the formula [1]:

$$l_{square} = \frac{d_{circ}}{2}\left(1 + \frac{1}{\sqrt{2}}\right) \tag{1}$$

The vias are then modeled with quadratic volume current basis functions (piecewise constant current in height) connecting the corresponding metallic sheets of one SIW waveguide with typically only one basis function per via. For multilayer microstrip-SIW transitions and other SIW components and circuits, we use a very effective modeling and discretization strategy [7].
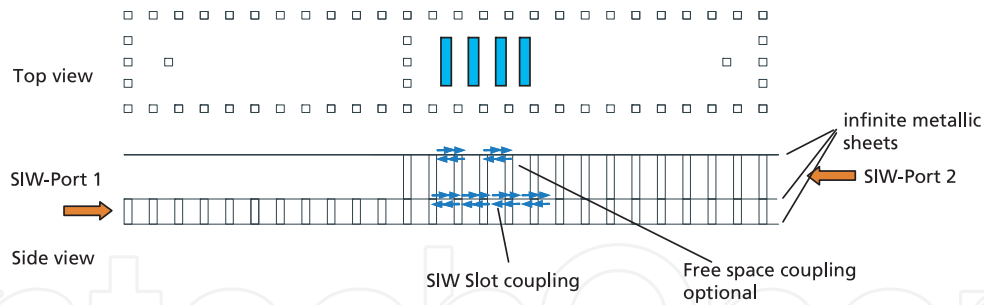
Figure 1. Structure with SI waveguides and ports on different levels with slot coupling as well as free space coupling (or a further stratified halfspace).
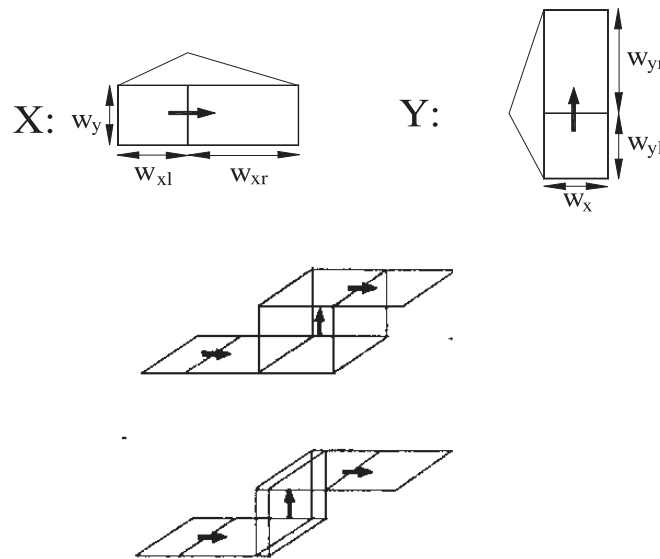

Figure 2. Used basis functions. Top: Planar (asymmetric) rooftop functions for electric and magnetic surface currents (x- and y-orientation). Bottom: z-directed volume currents attached to x-directed surface currents.

The SIWs are modeled with parallel-plate media where the metallic plates are connected by the vias of the SIW. A typical scheme, here with SIW waveguide ports, is given in **Figure 1**. It consists of two SI waveguides on different levels and SIW ports with a slot coupling (blue) and optional slots for the radiation in the upper half space, which can be free space or a complex stratified medium. As indicated in the side view, the slots are modeled with corresponding magnetic surface currents (also in blue) at the upper and lower side of the corresponding metallic sheet with opposite signs leading to a magnetic field integral equation for the magnetic currents. A sketch of the used basis functions is given in **Figure 2**.

For the matrix entries in the method of moments concerning magnetic surface current functions n and m on one level lb, we get a spectral admittance representation:

$$Y_{nm}(lb, lb) = \int_{k_x} \int_{k_y} \overleftrightarrow{G}^H_{M, lb, comp}(k_x, k_y, z_{lb}) \cdot \vec{F}_{lb, m}(k_x, k_y) \cdot \vec{F}^*_{lb, n}(k_x, k_y) dk_x dk_y \tag{2}$$

with the composite Green's function:

$$\overset{\leftrightarrow}{G}^H_{M,lb,comp}\left(k_x,k_y,z_{lb}\right) = \overset{\leftrightarrow}{G}^H_{M,lb}\left(k_x,k_y,z_{lb}\right) + \overset{\leftrightarrow}{G}^H_{M,lb-1}\left(k_x,k_y,z_{lb}\right)$$

which is the sum of the Green's functions $\overset{\leftrightarrow}{G}^H_{M,lb}$ above (radiation into a half-space or another parallel-plate medium) and below the metallic sheet lb (parallel-plate medium) $\overset{\leftrightarrow}{G}^H_{M,lb-1}$ and $\vec{F}_{lb,m,n}\left(k_x,k_y\right)$ the Fourier transforms of the basis functions. For the couplings between volume currents, we get a combined space/spectral impedance expression:

$$Z_{nk}\left(lv,lv'\right) =$$
$$\int_{k_x}\int_{k_y}\int_{z'}\int_z \overset{\leftrightarrow}{G}^E_{J,lb}\left(k_x,k_y,z',z\right)\cdot\vec{F}_{lv,k}\left(k_x,k_y,z'\right)\cdot\vec{F}^*_{lv,n}(k_x,k_y,z)dz\,dz'\,dk_x dk_y \quad (3)$$

with a complete analytical treatment of the space-domain integrations, and for couplings between magnetic and volume currents, we get a matrix entry without dimension, denoted with ZY:

$$ZY_{nk}(lv,lb) =$$
$$\int_{k_x}\int_{k_y}\int_{z'} \overset{\leftrightarrow}{G}^E_{J,lb}\left(k_x,k_y,z_{lb},z'\right)\vec{F}_{lv,k}\left(k_x,k_y,z'\right)\cdot\vec{F}^*_{lb,n}(k_x,k_y,z_{lb})\,dz'\,dk_x dk_y \quad (4)$$

The spectral domain integrations are carried out with two different strategies depending on the lateral distance of the basis functions.

A structure well suited for testing of different features of the method is given in **Figure 3**. At the right, we apply a SIW port 2 or a SIW absorber consisting of only five volume functions connected by lumped resistors with the metallic sheets.
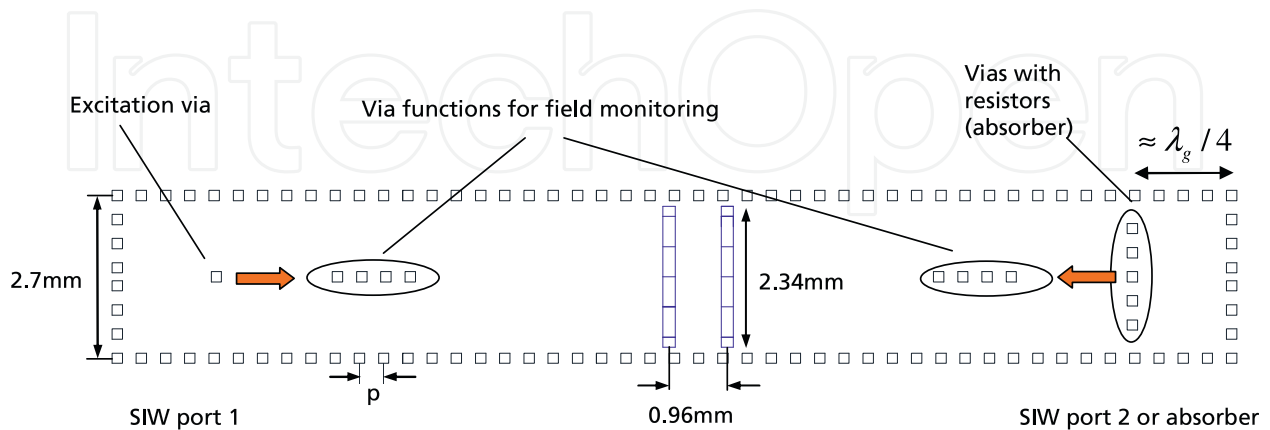

Figure 3. Structure for testing of SIW ports and absorbers combined with a reflection-canceling slot pair. Via side length 0.17 mm and via distance p = 0.4 mm, $\varepsilon_r = 3.0 - j0.003$, and h = 0.254 mm.

The SIW ports consist of an excitation via and four via (volume) functions here only used for field (voltage) monitoring in the center of the SIW to extract the forward and backward waves in the SIW for S-parameter calculation.

To compute the voltages at the field monitoring vias, at first the complete coupling matrix with all via functions is computed. Afterward the matrix is compressed by deleting the matrix columns related to the monitor functions and by taking out the related line entries stored for later reuse and the voltage computation. |S11|,tl and |S12|,tl are the results for the homogeneous through line with nearly an ideal matching and transmission showing the good performance of the SIW port model and S-parameter extraction. |S11|,abs shows the broadband matching with the 5-via absorber at the right using 240 Ohm resistors connecting the vias to the ground plane. Such an absorber can be used as an effective numerical broadband-matched termination of a SIW, but it should also be possible to manufacture it using SMD resistors connecting the vias with the ground planes.

For another test the SIW is fitted with two slots of length 2.34 mm in the middle. The separation and length of the slots are chosen in such a way that we get a so-called reflection-canceling slot pair. |S11|,ds denotes the matching with the additional reflection-canceling slot pair showing a quite good matching around 36–37 GHz.

A good test for the reliability of the numerical solutions and to get a detailed insight into the power flow of a structure is the computation of the power balance. Thus the input power at the excitation via (**Figure 3**) is

$$P_{IN} = \frac{1}{2}\text{Re}\{U \cdot I^*\} \tag{5}$$

The absorbed energy within the N_{abs} resistors with resistance R amounts to

$$P_{abs} = \frac{1}{2}\sum_{n=1}^{N_{abs}} R|I_n|^2 \tag{6}$$

And the radiated space wave energy into the upper halfspace is determined with the help of the saddle point method leading to the integral

$$P_{Rad} = \left| \frac{jk_m \cos\vartheta_r}{2\pi r} \int_{\vartheta_r=0}^{\pi/2} \int_{\varphi_r=0}^{2\pi} e^{jk_{xr} r \sin\vartheta_r \cos\varphi_r} e^{jk_{yr} r \sin\vartheta_r \sin\varphi_r} \overleftrightarrow{G}_M^{E,FF}\left(k_{xr}, k_{yr}\right) \sum_{n=1}^{N_s} I_n \overrightarrow{F}_n\left(k_{xr}, k_{yr}\right) r \sin\vartheta_r \, d\varphi_r d\vartheta_r \right|^2 \tag{7}$$

with the wavenumbers $k_{xr} = -k_m \sin\vartheta_r \cos\varphi_r$ and $k_{yr} = -k_m \sin\vartheta_r \sin\varphi_r$. Here k_m is the wavenumber of the topmost layer m and $\overleftrightarrow{G}_M^{E,FF}$ is the far-field evaluation of the Green's function for the electric field of magnetic (surface) currents radiating into layer m.

If the structures are analyzed with infinite low dielectric and metallic losses,

$$P_{IN} = P_{Rad} + P_{Abs} \qquad (8)$$

must hold. The results for the SIW with the absorber and the slot pair are given in **Figure 4**, right. It can be seen that the radiation power is below 20 percent up to about 37 GHz (the frequency band with good matching) with only one slot pair, whereas about 80 percent is converted in the absorber. If the input power according to Eq. (5) is normalized to 100 percent, then the sum in Eq. (8) leads to the red curve in **Figure 4**, right. Except some small deviation in the region 40–42 GHz, the 100 percent are met with good accuracy. However, for this accuracy the number of sampling points for the numerical integration must be quite high.

For an improved computational performance, a general coupling integral reads

$$V_{nm} = \iint\limits_{k_x \, k_y} \left[I \overleftrightarrow{G} \left(k_x, k_y, z_m, z_n\right) - I\overleftrightarrow{G}^{Asy} \left(k_x, k_y, z_m, z_n\right) \right] \cdot \vec{F}_{m0}\left(k_x, k_y. z_m\right) \cdot \vec{F}_{n0}^*\left(k_x, k_y, z_n\right) e^{jk_x \Delta x_{nm}} e^{jk_y \Delta y_{nm}} dk_x \, dk_y$$

$$+ \iint\limits_{k_x \, k_y} I\overleftrightarrow{G}^{Asy}\left(k_x, k_y, z_m, z_n\right) \cdot \vec{F}_{m0}\left(k_x, k_y. z_m\right) \cdot \vec{F}_{n0}^*\left(k_x, k_y, z_n\right) e^{jk_x \Delta x_{nm}} e^{jk_y \Delta y_{nm}} dk_x \, dk_y$$

$$(9)$$

where $I \overleftrightarrow{G}$ is a general Green's function tensor where all analytical space-domain integrations with regard to z and z' are already incorporated. The $\vec{F}_{m,n0}$ are the Fourier transforms of the basis functions in the origin of the coordinate system; thus, the Δx_{nm} and $\Delta y_{n,m}$ are the lateral separations of the basis functions with regard to x and y. **Figure 5** shows the different integration areas with the integrand behavior in the inner area A_{In} and the used simultaneous integration path deformations (for both wavenumbers k_x and k_y) in this area.

For basis functions with very small lateral separations or overlapping functions and self-couplings, an asymptotic representation $I\overleftrightarrow{G}^{Asy}$ for $k_\rho = \sqrt{k_x^2 + k_y^2} \to \infty$ is subtracted, leading to
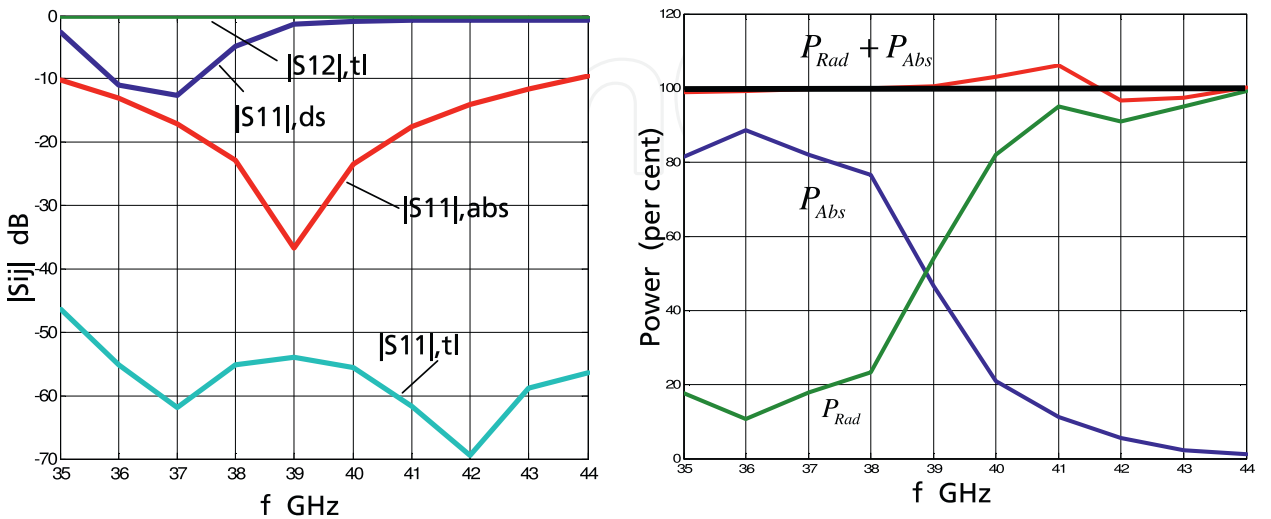

Figure 4. Left: S-parameter extraction results for the SIW through line (tl), with absorber (abs) and additional double slot (ds), h = 0.254 mm. Right: power balance.

an overall integrand with an exponential decay with regard to k_ρ. The contribution with this asymptotic representation is then added in Eq. (9) with the second integral, which can be evaluated completely analytically for all kinds of involved basis functions. In the inner area, pole rings due to surface wave and/or parallel-plate waves can occur; furthermore the inner area contains all wavenumbers related to radiating space waves. The wavenumbers in the outer areas A_{out1}, A_{out2}, and A_{out3} are mainly related to evanescent waves. However, if we have only SIW structures and components like in **Figure 3** without any radiating slots, we have only a contribution of a parallel-plate wave pole ring in the inner area for the coupling integrals of vias Eq. (3), whereas with a radiation by slots or other radiating elements into the upper (layered) halfspace, a branch point occurs as further singularity as well as possible surface wave poles in the integrands of the coupling integrals Eq. (2) and Eq. (4). All these
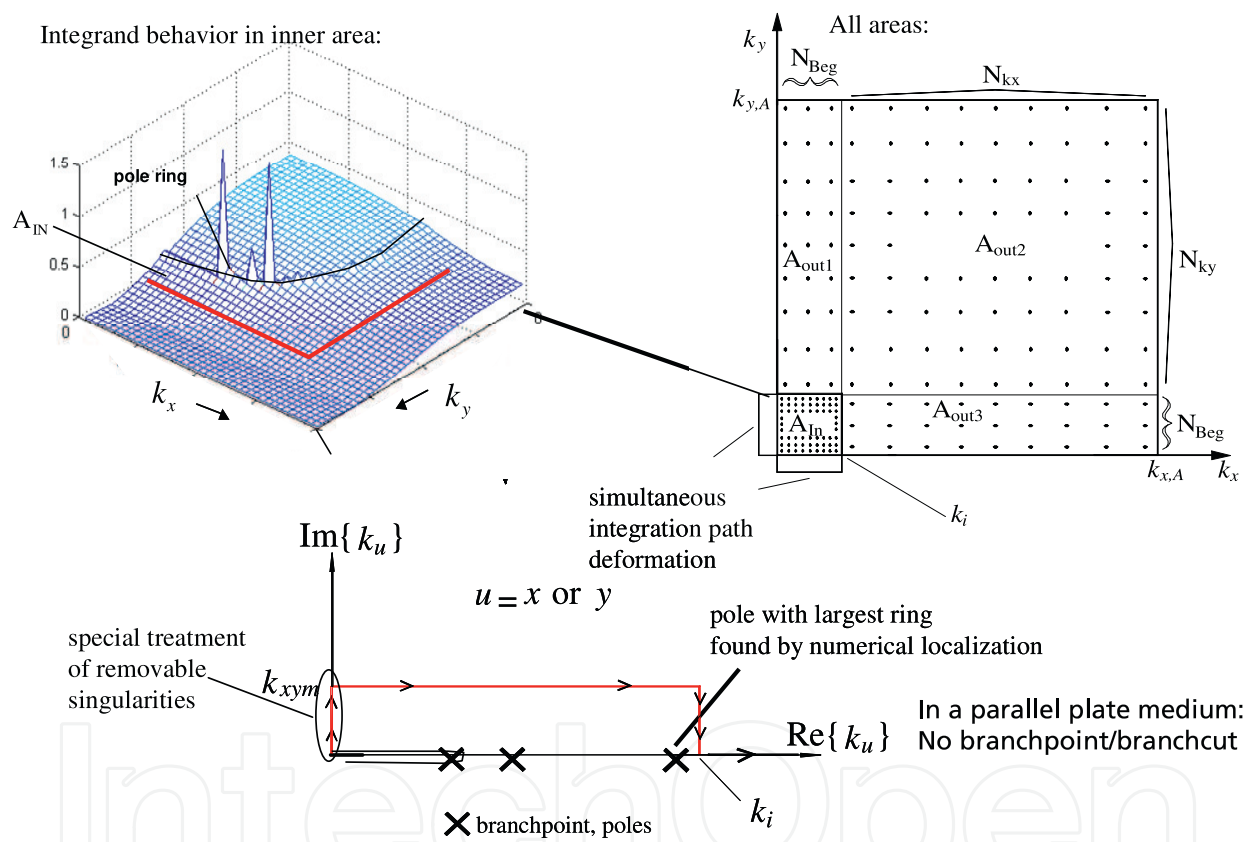

Figure 5. Top left: Typical integrand behavior in the inner integration area with pole rings. Right: First quadrant with all integration areas. Bottom: Simultaneous integration path deformations in the inner area.
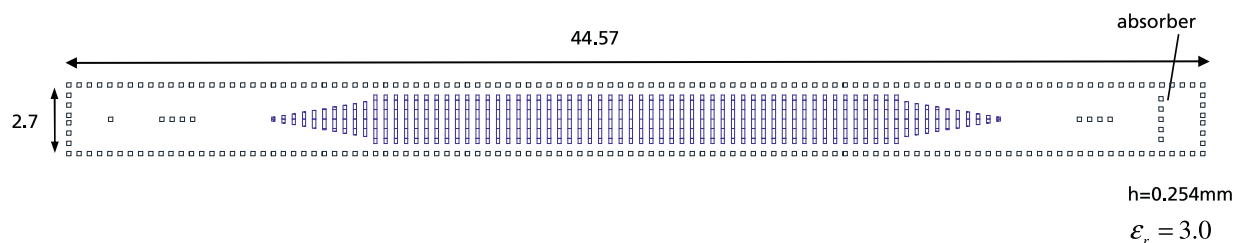

Figure 6. A leaky wave antenna with slots in the cover for end-fire radiation with the same SIW as in **Figure 3**. Slot separation 0.4 mm.

singularities are circumvented with the red integration path applied for both wavenumbers k_x and k_y(**Figure 5**, bottom). Since the only contribution in Eq.(3) for vias within the parallel plates comes from the parallel-plate wave pole, the number of integration sampling points in the inner area must be chosen significantly higher than typical microstrip and slot/coplanar
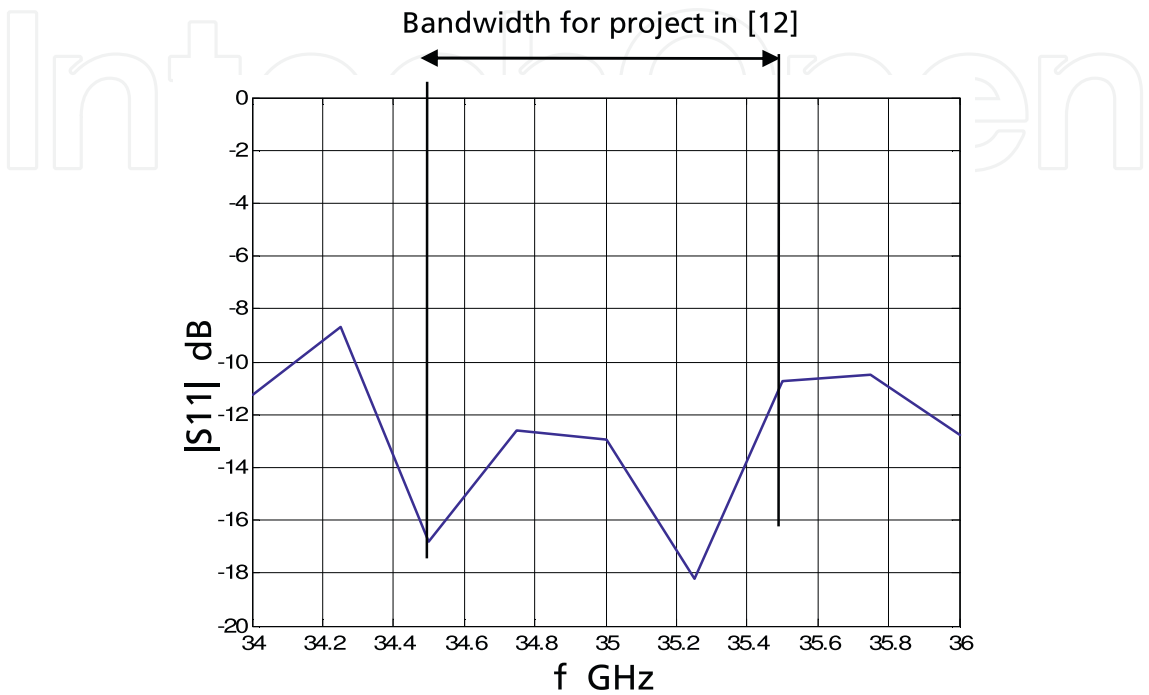

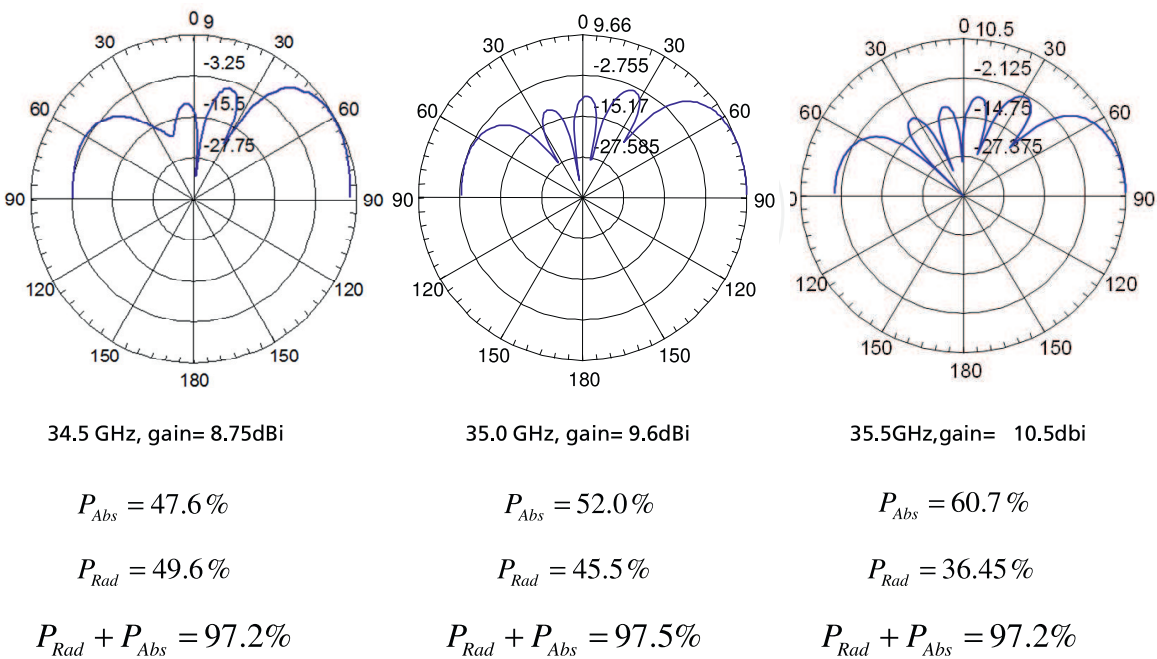**Figure 7.** Matching behavior of the structure in **Figure 6**.

| 34.5 GHz, gain= 8.75dBi | 35.0 GHz, gain= 9.6dBi | 35.5GHz,gain= 10.5dbi |

$$P_{Abs} = 47.6\%$$

$$P_{Rad} = 49.6\%$$

$$P_{Rad} + P_{Abs} = 97.2\%$$

$$P_{Abs} = 52.0\%$$

$$P_{Rad} = 45.5\%$$

$$P_{Rad} + P_{Abs} = 97.5\%$$

$$P_{Abs} = 60.7\%$$

$$P_{Rad} = 36.45\%$$

$$P_{Rad} + P_{Abs} = 97.2\%$$

Figure 8. Radiation patterns and power balance of the leaky wave antenna in **Figure 6**.

structures. For the structure in **Figure 3** with slots and absorber, 16 sampling points must be applied for both k_x and k_y wavenumbers on the horizontal path to reach the power balance accuracy in **Figure 4**, right. On the vertical paths, two sampling points for each path are sufficient. For the numerical integration, composite Legendre-Filon quadrature techniques are used.

A leaky wave antenna for end-fire radiation is given in **Figure 6** applying slots with constant length (l = 1.9 mm) in the middle and additional tapered slot areas at the ends for better matching. The simulated matching behavior is given in **Figure 7** together with the desired bandwidth for the MIMO radar project in [12].

A good test for the reliability of the results is to compute the sum of the absorbed power P_{abs} and the radiated power P_{rad} without dielectric losses. Thus we get for $P_{abs} + P_{rad}$ nearly constant values around 97.5% if the integration accuracy for Eqs. (2)–(4) is sufficient. This is outlined in **Figure 8** for three frequencies together with the antenna elevation patterns.

3. Microstrip to SIW transitions

For the connection of structures like in **Figure 6** to a microstrip circuitry, a microstrip-SIW transition like in **Figure 9** is well suited, consisting of a microstrip line with width w_{mic} (0.33 mm) on a substrate with the height h_{Mic} (here 0.13 mm). The energy of the microstrip line is then coupled by the via (with distance d to the left wall, here 1.49 mm) through the antipad (blue, side length 0.42 mm) into the SIW with the height h_{SIW} (0.75 mm) and width w_{SIW} (4.29 mm).

The permittivity for both the microstrip line and the SIW is $\varepsilon_r = 3.0$. The incident (i_i) and backward (i_b) current waves on the microstrip line are extracted by means of the complex amplitudes of four current basis functions. The voltage waves in the SIW u_i and u_b are extracted by means of four electric field monitors in the same way as in **Figure 3**.
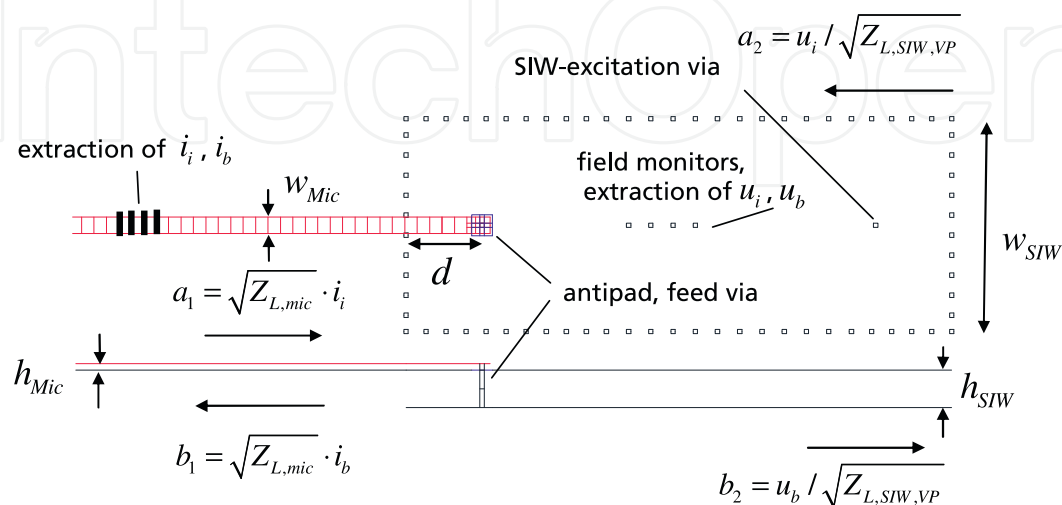

Figure 9. Extraction of the S-parameter for a microstrip-SIW transition.

For the consistent evaluation of the wave quantities a_1, b_1, a_2, b_2, it is necessary to use the voltage-power definition for the characteristic impedance for the microstrip line and especially for the SIW. With the help of the equivalent width of a SIW:

$w_{eq} = w_{SIW} - \frac{d_{circ}^2}{0.95\,p}$ (see, e.g. [3] and d_{circ} from Eq. (1)) and p the center to center distance of the vias we get for the characteristic impedance:

$$Z_{L,SIW,VP} = 2\frac{h_{SIW}}{w_{eq}}\frac{\mu_0\omega}{\sqrt{k^2 - \left(\frac{\pi}{w_{eq}}\right)^2}} = \frac{|U|^2}{2P_{w,a,b}} \tag{10}$$

Figure 10 shows the results with the own IG-approach and with the time domain approach of CST Microwave Studio both with a very similar behavior. The green curve for $|S_{11}|$ in the own IG-approach is for a finer vertical discretization (three volume basis functions), whereas the other curves are computed with two volume basis functions showing already a stable solution behavior for this configuration. For $|S_{22}|$ we get nearly the same results as for $|S_{11}|$ as expected due to the very low dielectric losses considered for the simulation in contrast to the results with CST MWS. Structures like in **Figure 9** with a small thickness of the SIW can be designed with the formulas, e.g., in [6]. For the input resistance, we get

$$R_{in} = 2 \cdot \frac{k_0\ h_{SIW}\ Z_0}{w_{eq}\ \beta_{10}} \sin^2(\beta_{10}d)\sin^2\left(\frac{\pi x}{w_{eq}}\right) \tag{11}$$

with k_0 and Z_0 the free space wave number and wave impedance, respectively, and β_{10} the propagation constant in the filled equivalent rectangular waveguide. Typically, the feed via is centered in the SIW, i.e., $x = w_{eq}/2$ and d is around a quarter of a guided wavelength and h_{SIW} should be much smaller than a quarter of a guided wavelength to guarantee a nearly constant current distribution on the feed via. In contrast to the formula in [6], Eq. (11) has an additional
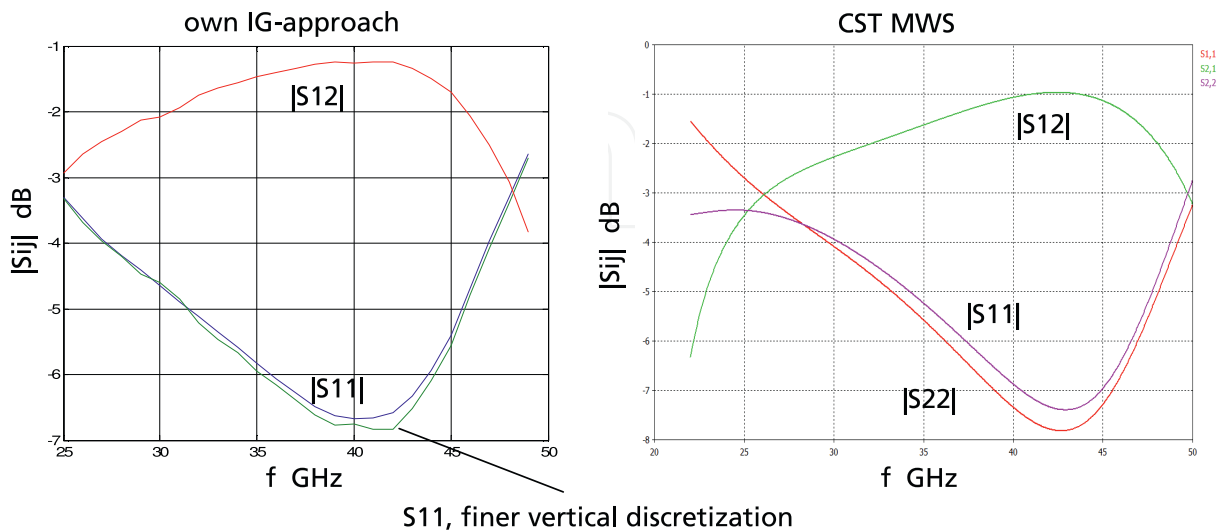

Figure 10. Results for the structure in **Figure 9**. Left: With own IG-approach. Right: With CST Microwave Studio (time domain).

factor of 2 due to a mistake during the derivation in [6]. For small values of h_{SIW}, the structure in **Figure 9** can be further optimized, and a broadband matching can be achieved with a microstrip circuitry as shown in the following structure. For larger values h_{SIW}, the structure in **Figure 11** is much better suited for broadband operation.

In this case the feed via has only a length of 1.0 mm within the SIW with a height of 2.5 mm. Again the permittivity for both the microstrip line and the SIW is $\varepsilon_r = 3.0$. Such a structure is similar to a coaxial probe feed in a rectangular waveguide; thus, a start design can be made with solution methods like in [6], modified for filled waveguides. However, the influence of the antipad and optional pad structure typically has a significant influence on the overall impedance seen from the microstrip line. Therefore we started directly with numerical tests using typical values for pad and antipad size as well as for the length and the side length (here 0.43 mm) of the feed via. The other vias have a side length of 0.26 mm with a separation of 1 mm. This leads for the configuration in **Figure 11** (without the matching stubs) in a short time to a design with the behavior in **Figure 12**, left. For the structure in **Figure 11**, only 311 basis functions are needed with a computation time of about 1 minute for 34 frequency points (AMD Phenom II X4 965 Quadcore processor). For the vertical discretization, six volume basis functions are used for each via of the SIW and the feed via to achieve stable results.

In this case, an additional pad did not show a further improvement, but with the shape of the antipad (blue), a further slight optimization could be performed, leading to a length of 0.9 mm and a width of 0.7 mm. However, with these specifications, we not yet achieve a matching below -10 dB in the desired frequency range from 30 to 40 GHz, but we get a flat curve between -7 and -8 dB for $|S_{11}|$. Based on this behavior, a further matching with two additional microstrip stubs leads to the behavior in **Figure 12**, right, now showing a good matching from less than 30 GHz to more than 40 GHz. **Figure 13** shows the matching with a SIW absorber at the right end of the SIW in **Figure 11**. In this case the absorber has a slightly smaller bandwidth than the transition.

Besides this kind of transition, we have also specified transitions with a stepwise ridged waveguide. These structures are similar than the proposed transitions in [4], but we do not need the quite complex tapered shapes described in [4]. Our design is based on a two-stage Chebychef approach which can handle also much higher transform ratios than the designs in [6].
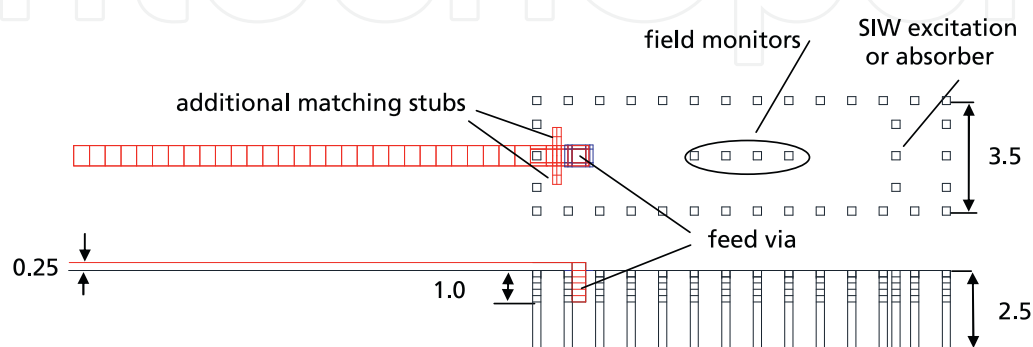

Figure 11. Broadband microstrip-SIW transition for SIWs with larger thickness.
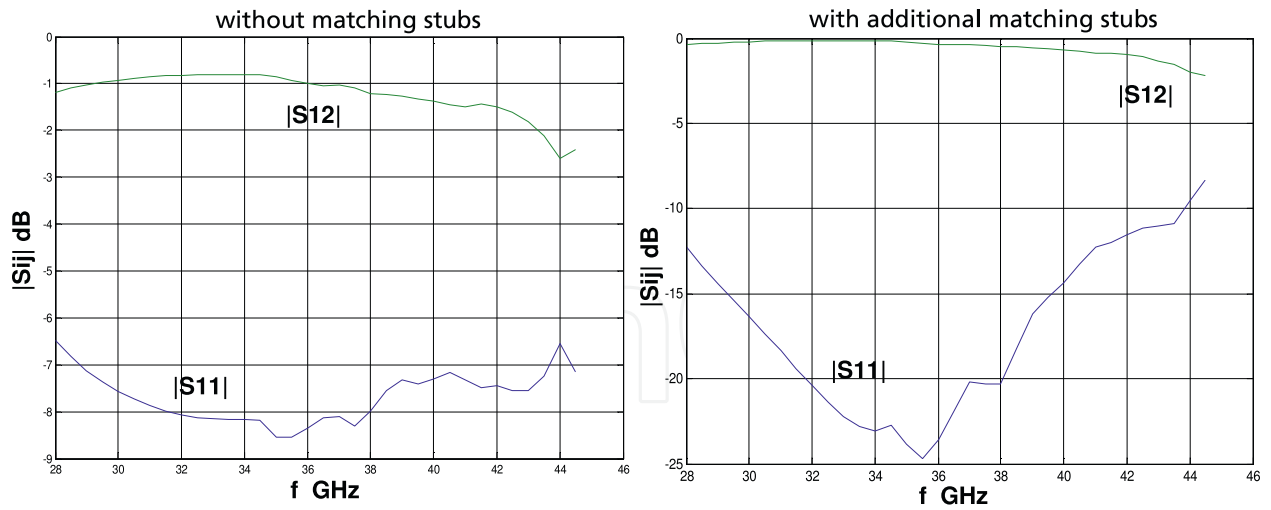
Figure 12. Results for the structure in **Figure 11** with microstrip port to the left and SIW port to the right. Left: Without matching stubs. Right: With additional matching stubs.
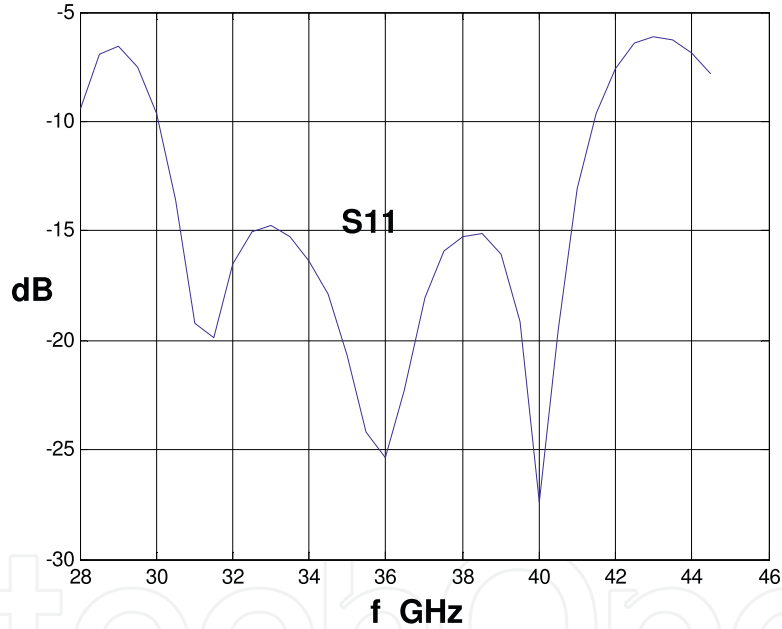

Figure 13. Result for the structure in **Figure 11** with SIW absorber to the right.

A typical design with our approach is given in **Figure 14**. Here, the transform ratio with the definition

$$\alpha = \frac{\text{hrw-hmic}}{\text{hrw}}$$

amounts to 7, whereas in [4], only a structure with a transform ratio of 4 was designed. **hrw** is the height of the standard SIW (or rectangular waveguide to the right) and **hmic** is the height of the microstrip line to the left.
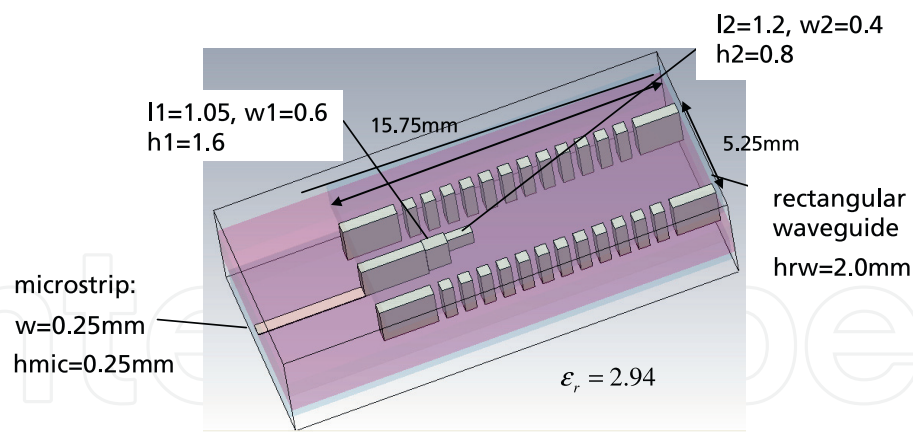
Figure 14. Design of a microstrip-SIW transition with two-stage ridged waveguide. Dimensions in mm.
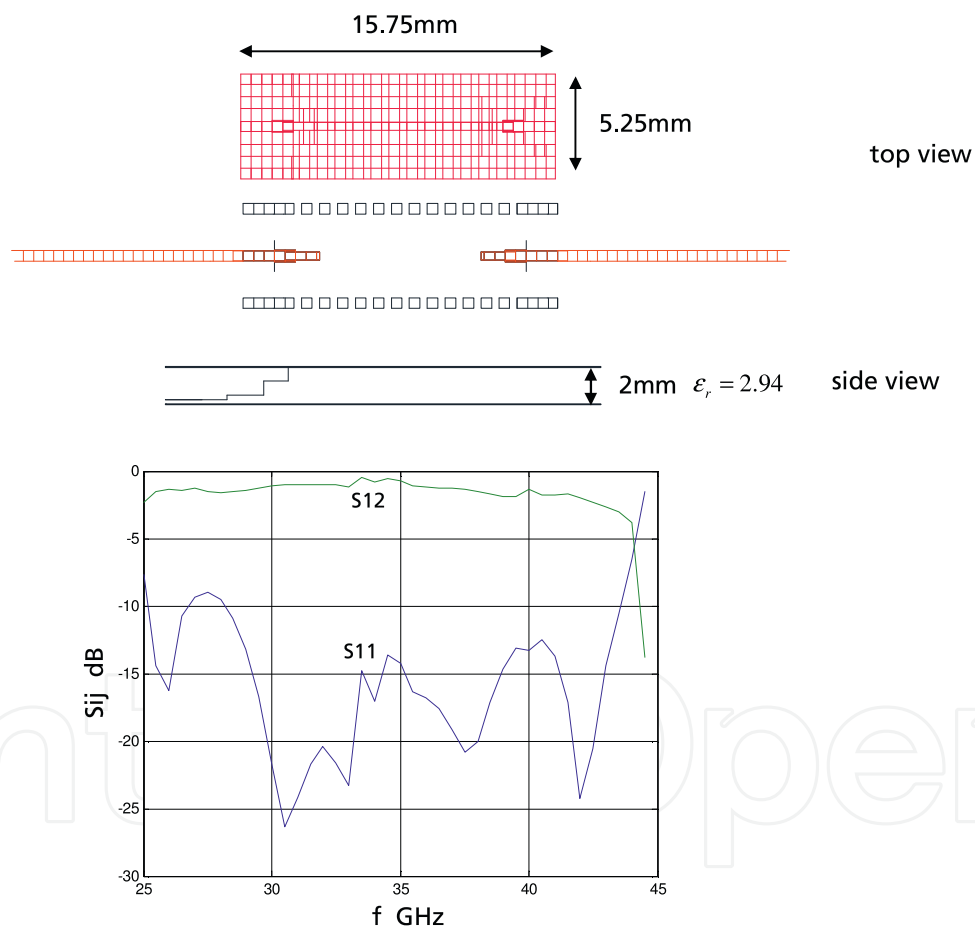

Figure 15. Microstrip to SIW transition with two-stage ridged waveguide. Top: Back-to-back arrangement with discretization. Bottom: S-parameter (absolute values).

For the design of the transition, a quantity

$$\sec\Theta_m = \cosh\left(\frac{1}{2}\cosh^{-1}\left|\frac{\ln(Z_{SIW}/Z_{mic})}{2 \cdot a_{rip}}\right|\right)$$

is computed, where Z_{SIW} is the characteristic impedance of the SIW or the equivalent rectangular waveguide, here the voltage-power definition Eq. (10) should be used, and Z_{mic} the characteristic impedance of the microstrip line. With this quantity, two reflection factors are computed with

$$\Gamma_0 = \frac{a_{rip}}{2} \sec^2(\Theta_m), \quad \Gamma_1 = a_{rip}\left(\sec^2(\Theta_m) - 1\right)$$

where a_{rip} is the tolerated intensity of the ripples in the passband, e.g., for 10 percent, $\alpha_{rip} = 0.1$. With $Z_{SIW} = 258$ Ohm and $Z_{mic} = 47$ Ohm, we get $\sec\Theta_m = 2.18$. With the reflection factors, we can compute the characteristic impedances for the ridged waveguide sections:

$$Z_1 = Z_{mic} \cdot e^{2\Gamma_0}, \quad Z_2 = Z_1 \cdot e^{2\Gamma_1}$$

leading here to $Z_1 = 74.45$ Ohm and $Z_2 = 161$ Ohm. To determine the corresponding ridged waveguide dimensions, we have used CST MWS to compute the voltage from the ridge to the lower ground for a given power. This leads to the dimensions **l1, w1,** and **h1** for length, width, and height of the first section and **l2, w2,** and **h2** for the second section as also given in **Figure 14**. For the section which is connected with the microstrip line, we have chosen the same width as for the microstrip line because the differences of the characteristic impedances remain small. Of course a further adjustment of this width can be done. **Figure 15**, top, shows the transition in a back-to-back arrangement together with the discretization for our integral equation approach (side view shows only the first transition). In this case, we have modeled the cover of the SIW as a finite structure, whereas the bottom ground plane remains infinite.

4. SIW horn antenna elements

Figure 15, bottom, shows the matching behavior of this arrangement. The reflection factor remains mainly below -15 dB; the structure may be a good alternative to the transition in **Figure 11**. The back-to-back structure was also built and measured successfully and was then combined with two radiating apertures shown in **Figure 16**. On the left the transition is combined with a simple open SIW and a short parallel-plate section. On the right an additional stepwise widening is applied. This is realized with two dielectric bars which are glued on the top and bottom side of the parallel-plate section where the metallization was removed before at these areas. As shown in the inset in **Figure 16**, the upper dielectric bar is metallized at the top and at the left side and analogously the lower bar to get a symmetric aperture with a height of 3.5 mm.

For the characterization of such structures with an end-fire radiation, we use CST Microwave Studio (time domain solver) at the moment, because it is still difficult with our integral equation framework to handle structures with finite dielectric layers to one side [5].

Figure 17 shows left the simulated matching behavior of the two structures. With the simple open SIW, the matching is still very poor as expected (blue line), whereas with the additional widening, the reflection factor remains below -10 dB for a large frequency range. However, despite of the additional widening, we still get a rather strong backward radiation as illustrated
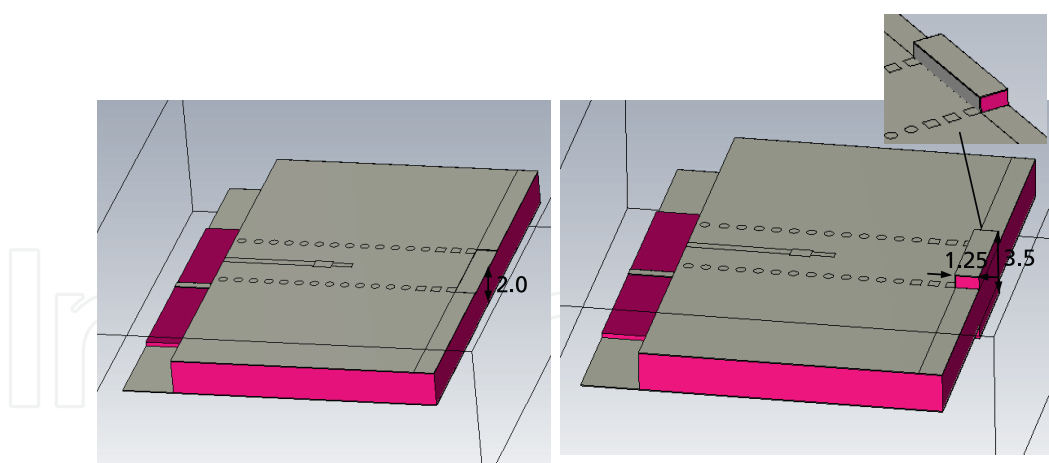
Figure 16. Combinations of the transition in **Figure 15** with two radiating apertures. Left: Open SIW with short parallel-plate section. Right: With a stepwise widening at the end.
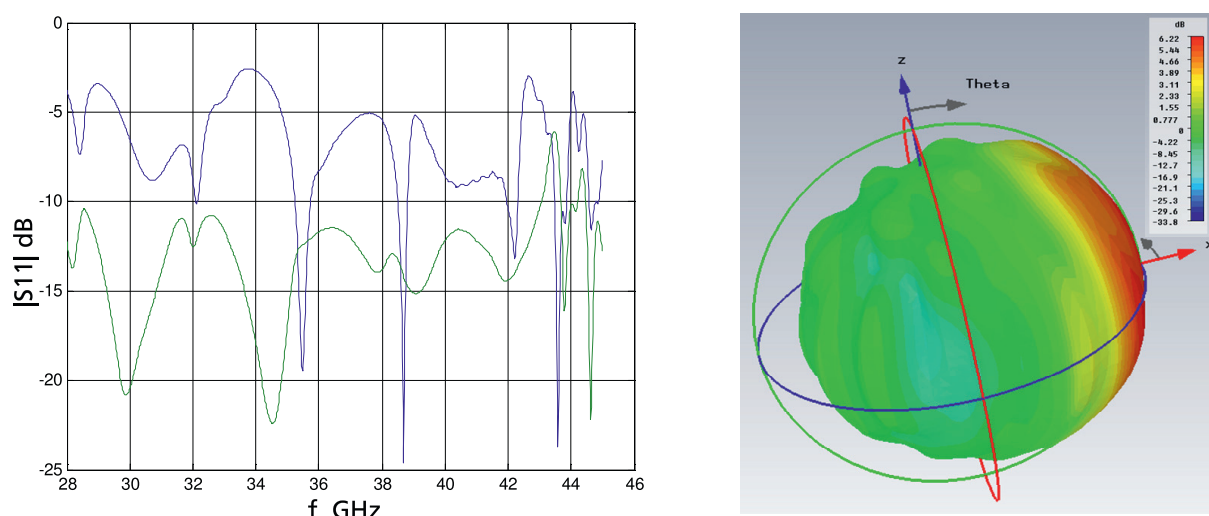

Figure 17. Left: Matching behavior of the structures in **Figure 16**. Blue: Open SIW and parallel-plate section. Green: With widening. Right: Antenna pattern (gain) of the structure with widening. Simulations with CST MWS.

in **Figure 17**, right. The structures were manufactured and measured afterward showing the matching behavior in **Figure 18** with the screenshots of the network analyzer. Similar as the simulated results, the simple structure with open SIW shows a poor matching around −5 dB up to the dip around 33.8 GHz, whereas the structure with widening shows a good matching mainly below −10 dB over the whole measured frequency range. Despite of the good matching behavior and further options to reduce the backward radiation, the stepwise widening is difficult to fabricate, even in the case it is designed with via wholes like the feeding SIW.

SIW horn antennas have already been studied for a longer time; typically they suffer from the substrate to the air transition which leads to larger reflections and backside radiation especially with thin substrates as we have seen with the open SIW aperture in **Figure 16**. In [9], a better matching and bandwidth enhancement of such kind of antennas is achieved with several parallel-plate sections in front of the origin antenna. However, the problem with the large
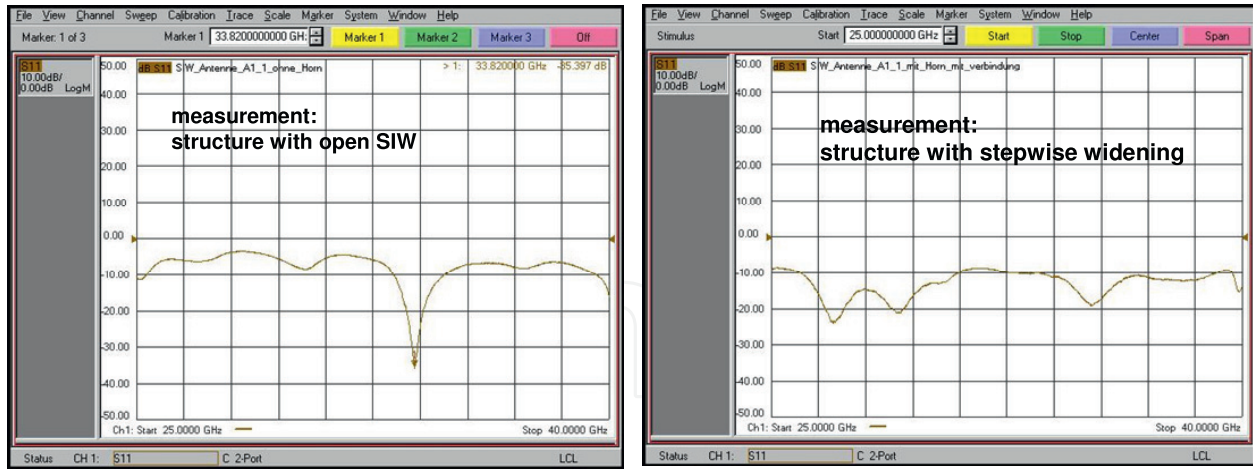
Figure 18. Measured matching behavior of the structures in **Figure 16**. Left: Open SIW and parallel-plate section. Right: With widening.
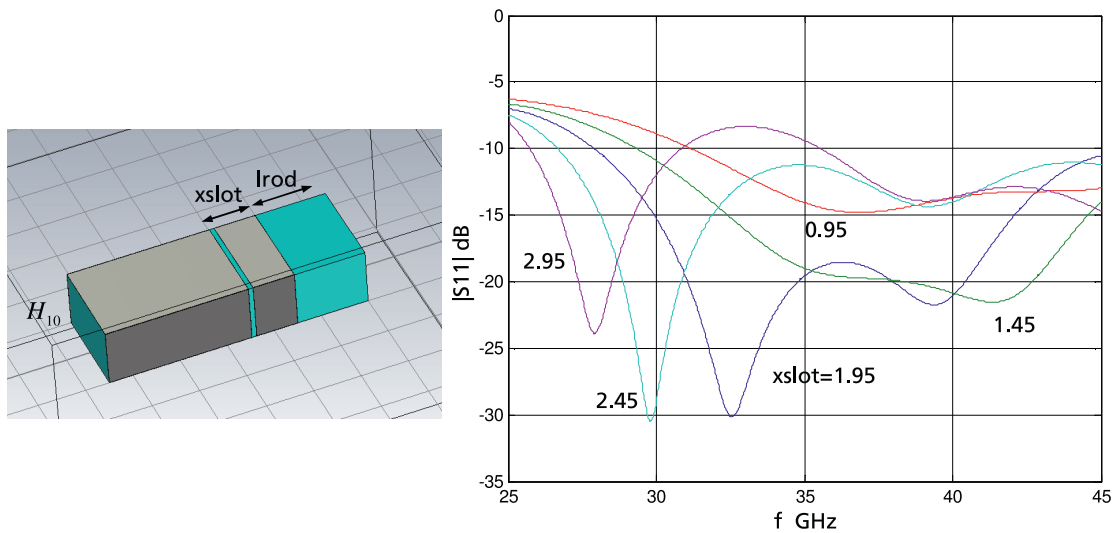

Figure 19. Left: Rectangular waveguide with ringslot and dielectric rod. Right: Matching behavior of the left structure in dependence of **xslot** (in mm) and **lrod** fixed to 2.5 mm (CST MWS).

backside radiation is only slightly reduced or not at all; typically, a good matching is achieved but simultaneously with a large backside radiation and vice versa. Some further improvements are made in [10] using transitions with a saw-tooth geometry. But for a good performance, the aperture width must be typically larger than one free space wavelength; thus, an application within a typical phased array arrangement requiring an element distance around $\lambda_0/2$ is not possible.

In contrast to the parallel-plate configurations in [9, 10] or the widening in **Figure 16**, right, for a better matching of SIW horn antennas, we use in a further study a (rectangular) ringslot to improve the matching behavior and bandwidth together with a reduction of the backside radiation. **Figure 19** shows the structure with the rectangular ringslot located with the distance **xslot** apart from the right metallic edge of the rectangular waveguide and a dielectric extension with the length **lrod** (fixed to 2.5 mm). The width of the waveguide and dielectric is set to 4.0 mm, the height to 2.0 mm. This means that the width is only slightly higher than $\lambda_0/2$ at
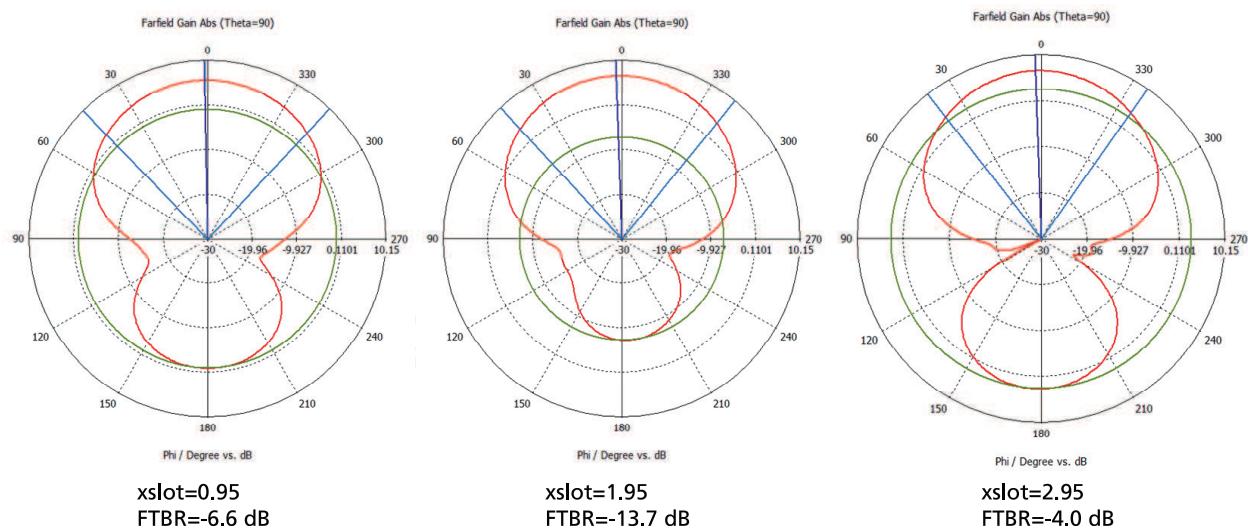
Figure 20. Azimuth diagrams at 35 GHz and FBTR for three values of **xslot**.

35 GHz. At the right the matching behavior of the structure with H_{10} wave excitation and variation of **xslot** is illustrated. With a desired center frequency of 35 GHz and a bandwidth with a range of 30 to 40 Ghz at least, a value of 1.95 mm for **xslot** is best suited in this context.

The dependence of the matching behavior with regard to **lrod** and the slot width is much lower; in this case, a slot width of 0.2 mm was used. **Figure 20** shows the azimuth diagrams for three values of **xslot** together with the forward-to-backward ratio (FTBR). It can be observed that the best value is reached for xslot = 1.95 mm, which also leads to the best matching behavior.
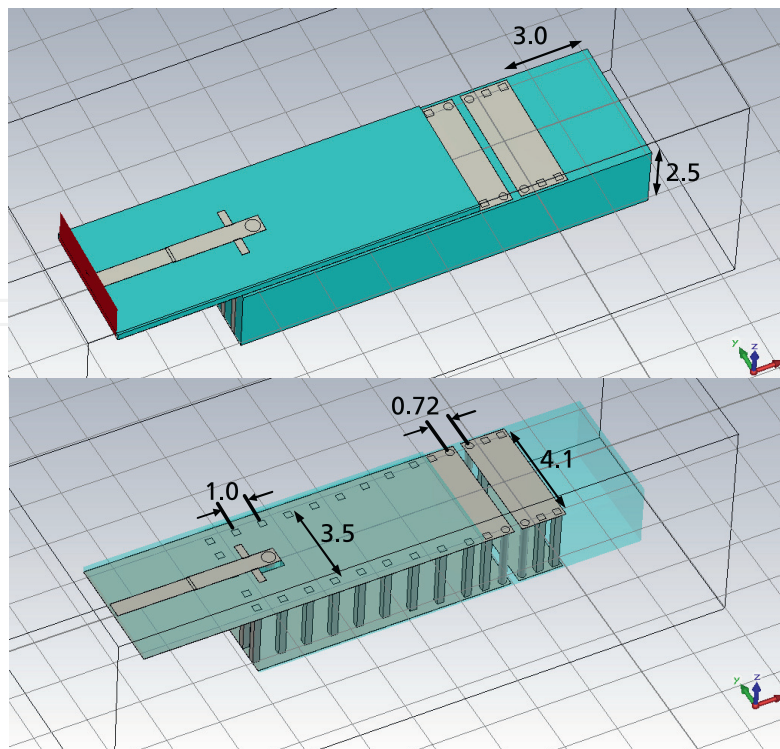

Figure 21. Complete antenna element in SIW technology. Top: Representation with hidden components. Bottom: With transparent substrates. Dimensions in mm.

The structure in **Figure 19** has then been transformed into SIW technology and combined with the microstrip to SIW transition of **Figure 11** with the substrate thickness 2.5 mm. This leads to the structure in **Figure 21**. The slot width in the lower and upper metallization amounts to 0.3 mm; the via separation near the slot was reduced to 0.72 mm. In the region of the feeding via, the SIW has a width of 3.5 mm as in **Figure 11** (center to center of the vias) and is then increased by a smooth taper to 4.1 mm.

The vias close to the slot are modeled with a round cross section, but the differences compared with a quadratic cross section are negligible.

Figure 22 shows the matching behavior simulated with CST. We can see that the reflection factor is even below −15 dB in the range from 30 to 40 GHz.

Finally, **Figure 18** shows the antenna patterns derived with CST MWS. Especially by hands of the 3D pattern, we can observe that the overall backside radiation is very low. A similar antenna element like in **Figure 21** was already built, but in the microstrip-to-SIW transition, the feeding via is connected with the bottom ground plane like in **Figure 9** leading therefore to a (desired) smaller bandwidth of about 2 GHz around the center frequency 35 GHz well suited for the project in [12] mentioned in context with the leaky wave antenna in **Figures 6** and **7**. The fabricated elements show a similar antenna pattern than in **Figure 23** and are already tested in a phased array arrangement.
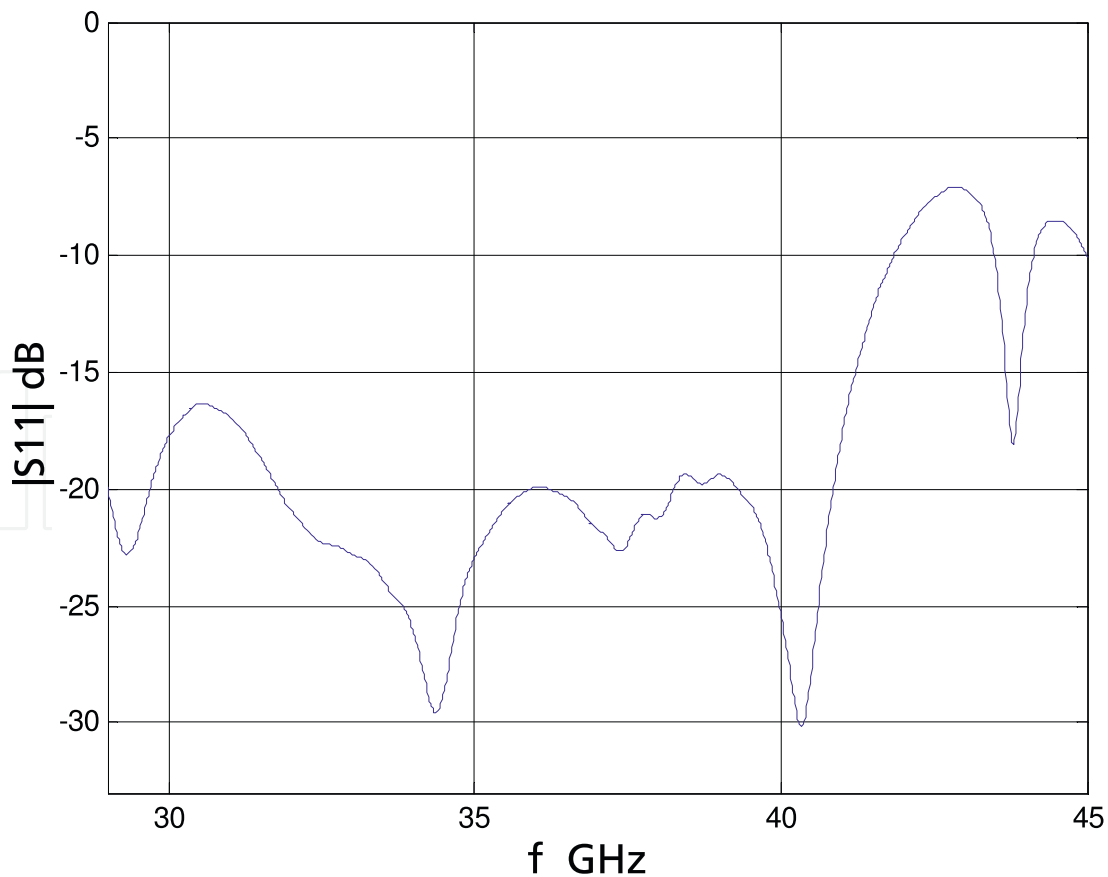

Figure 22. Left: Matching behavior of the complete antenna element in **Figure 21** (CST MWS). Right: Fabricated element (here for the project in [12]), top view with microstrip line and matching stubs and bottom view with 1 Euro coin.
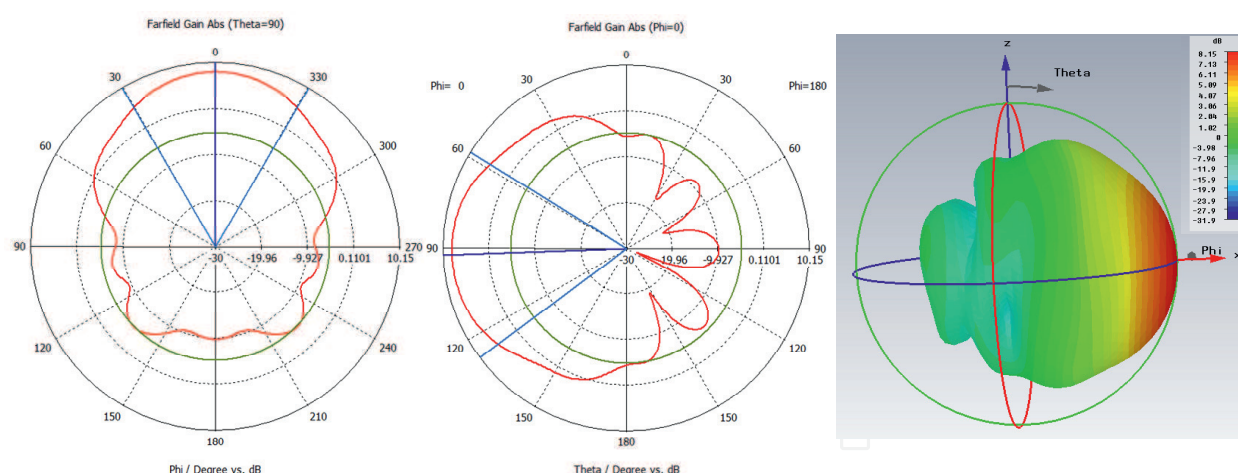
Figure 23. Azimuth, elevation, and 3D antenna pattern of the antenna element in **Figure 21** at 35 GHz.

5. Conclusions

This chapter comprises the application of an integral equation framework to the analysis and design of substrate integrated waveguide (SIW) components and antennas. For SIW circuits, microstrip to SIW transitions, and slot antennas, only the vias must be considered for the discretization of the SIWs in many cases, whereas radiating slots or antipads are modeled with magnetic surface currents. The computational performance and accuracy are significantly improved by a subdivision of the Cartesian wavenumber plane, integration path deformations, an asymptotic subtraction technique, as well as extended quadrature methods. The introduction of special SIW ports, field monitoring, and compact SIW absorbers allows an effective S-parameter extraction and power balance control also in combination with microstrip ports. For SIWs with larger thickness, broadband microstrip-to-SIW transitions have been designed based on a feed via with pad/antipad combination and a two-stage ridged-SIW structure. The latter was combined with an end-fire horn antenna based on a stepwise widening and was successfully built and measured. But the best radiation properties could be obtained with a combination of a SIW with a rectangular ringslot and a dielectric rod showing both broadband behavior and a small backward radiation. This structure is already tested within different array arrangements for a MIMO radar using a transition with feed via connected to the lower ground and smaller bandwidth, whereas a broadband version is used in near future for an airborne synthetic aperture radar.

Author details

Thomas Vaupel

Address all correspondence to: thomas.vaupel@fhr.fraunhofer.de

Fraunhofer Institute for High Frequency Physics and Radar Techniques FHR, Wachtberg, Germany

References

[1] Buchta M, Heinrich W. On the equivalence between cylindrical and rectangular via-holes in electromagnetic modeling. In: Proceedings of the 37th EuMC. Oct. 2007:142-145

[2] Caballero ED, Esteban H, Belenguer A, et al. Efficient analysis of substrate integrated waveguide devices using hybride mode-matching between cylindrical and guided modes. IEEE Transactions on Microwave Theory and Techniques. Feb. 2012;**60**(2):232-243

[3] Kumar H, Jadhav R, Ranade S. A review on substrate integrated waveguide and its microstrip interconnect. IOSR Journal of Electronics and Communication Engineering. Sep-Oct. 2012;**3**(5):36-40

[4] Ding Y, Wu K. Substrate integrated waveguide-to-microstrip transition in multilayer substrate. IEEE Transactions on Microwave Theory and Techniques. Dec. 2007;**55**(12):2839-2844

[5] Vaupel T. Design of end-fire substrate integrated waveguide antenna elements using in-house planar-3D integral equation frameworks and commercial full-3D methods. In: 8th European Conference on Antennas and Propagation. Netherlands: The Hague; 2014:2512-2515

[6] Yau CK, Huang TY, Shen TM, et al. Design and modelling of microstrip line to substrate integrated waveguide transitions. In: Zhurbenko V, editor. Passive Microwave Components and Antennas. InTechOpen. April 2010:225-246. Chapter 11. DOI: 10.5772/9418 ISBN: 978-953-307-083-4

[7] Vaupel T. A MFIE/Volume integral equation approach with minimum discretization effort for substrate integrated waveguide structures and leaky wave/slot antennas. IEEE APS Symposium. Fajardo, Puerto Rico; 2016:1327-1328

[8] Liu J, Jackson D, Long Y. Substrate integrated waveguide (SIW) leaky-wave antenna with transverse slots. IEEE Transaction on Antennas and Propagation. Jan 2012;**60**(1):20-29

[9] Esquis-Morote M, Fuchs B, Zürcher J-F, Mosig JR. A printed transition for matching improvement of SIW horn antennas. IEEE Transactions on Antennas and Propagation. April 2013;**61**(4):1923-1930

[10] Esquis-Morote M, Fuchs B, Zürcher J-F, Mosig JR. Novel thin and compact H-Plane SIW horn antenna. IEEE Transactions on Antennas and Propagation. June 2013;**61**(6):2911-2920

[11] Vaupel T, Eibert TF, Hansen V. Spectral domain analysis of large (M)MIC-structures using novel quadrature methods. International Journal of Numerical Modelling: Electronic Networks, Devices and Fields. Jan-Feb. 2005;**18**:23-38

[12] Panhuber R, Klenke R, Biallawons O, Klare J. System concept for the Imaging MIMO Radar of the radar warning and information System RAWIS. In: Proceedings of EUSAR 2016: 11th European Conference on Synthetic Aperture Radar. Hamburg, Germany. 2016:1-4